nanomaterials

MDPI

Article

Surfactant Tween 20 Controlled Perovskite Film Fabricated by Thermal Blade Coating for Efficient Perovskite Solar Cells

Kun-Mu Lee [1,2,3,4,*,†], Shun-Hsiang Chan [1,2,*,†], Chang-Chieh Ting [5], Shih-Hsuan Chen [1], Wei-Hao Chiu [4], Vembu Suryanarayanan [6], Jen-Fu Hsu [3], Ching-Yuan Liu [5,*] and Ming-Chung Wu [1,2,3,*]

1 Department of Chemical and Materials Engineering, Chang Gung University, Taoyuan 33302, Taiwan; cgu.shihhsuanchen@gmail.com
2 Green Technology Research Center, Chang Gung University, Taoyuan 33302, Taiwan
3 Division of Neonatology, Department of Pediatrics, Chang Gung Memorial Hospital, Linkou, Taoyuan 33305, Taiwan; hsujanfu@cgmh.org.tw
4 Center for Reliability Sciences and Technologies, Chang Gung University, Taoyuan 33302, Taiwan; d0000017236@cgu.edu.tw
5 Department of Chemical and Materials Engineering, National Central University, Jhongli District, Taoyuan 32001, Taiwan; kero5206@gmail.com
6 Electroorganic and Materials Electrochemistry Division, CSIR-Central Electrochemical Research Institute, Karaikudi 630003, India; vidhyasur@yahoo.co.in
* Correspondence: kmlee@mail.cgu.edu.tw (K.-M.L.); shunhsiangchan@gmail.com (S.-H.C.); cyliu0312@ncu.edu.tw (C.-Y.L.); mingchungwu@cgu.edu.tw (M.-C.W.)
† These authors contributed equally to this work.

Abstract: In recent years, additive engineering has received considerable attention for the fabrication of high-performance perovskite solar cells (PSCs). In this study, a non-ionic surfactant, polyoxyethylene (20) sorbitan monolaurate (Tween 20), was added as an additive into the $MAPbI_3$ perovskite layer, and the thermal-assisted blade-coating method was used to fabricate a high-quality perovskite film. The Tween 20 effectively passivated defects and traps in the $MAPbI_3$ perovskite films. Such a film fabricated with an appropriate amount of Tween 20 on the substrate showed a higher photoluminescence (PL) intensity and longer carrier lifetime. At the optimal concentration of 1.0 mM Tween 20, the performance of the PSC was apparently enhanced, and the champion PSC demonstrated a PCE of 18.80%. Finally, this study further explored and compared the effect on the device performance and ambient stability of the $MAPbI_3$ perovskite film prepared by the spin-coating method and the thermal-assisted blade coating.

Keywords: perovskite solar cells; surfactant Tween 20; thermal-assisted blade coating; power conversion efficiency

check for updates

Citation: Lee, K.-M.; Chan, S.-H.; Ting, C.-C.; Chen, S.-H.; Chiu, W.-H.; Suryanarayanan, V.; Hsu, J.-F.; Liu, C.-Y.; Wu, M.-C. Surfactant Tween 20 Controlled Perovskite Film Fabricated by Thermal Blade Coating for Efficient Perovskite Solar Cells. *Nanomaterials* **2022**, *12*, 2651. https://doi.org/10.3390/nano12152651

Academic Editor: Efrat Lifshitz

Received: 11 July 2022
Accepted: 28 July 2022
Published: 2 August 2022

Publisher's Note: MDPI stays neutral with regard to jurisdictional claims in published maps and institutional affiliations.

1. Introduction

Over the past decade, metal halide perovskite solar cells (PSCs) have resulted in tremendous interest in the next generation of solar cell technologies, benefiting from their high absorption coefficient [1–5], ever-increasing photoelectric characteristics [6,7], low-cost materials [8,9], simple fabrication process [10], and so on. The typical three-dimensional (3D) perovskite structure is represented by the ABX_3 structure, where A is a monovalent cation, B is a divalent metal cation, and X is a halide anion [11]. Because the perovskite films are known to exhibit unavoidable defects that act as charge recombination centers, the defects could deteriorate charge carrier transport and collection and hinder the performance improvement of the devices. Recently, many scientists have devoted themselves to studying PSCs by optimizing the perovskite layer and the interface between each layer to achieve high power conversion efficiency (PCE), which has exceeded 25% in the last decade.

To obtain high-performance and stable perovskite devices, controlling the morphology [12,13], grain boundary [14], grain size, charge recombination [15], and the density

of the defect states in the perovskite film are necessary [16]. Therefore, how to prepare a high-quality, uniform, and pinhole-free perovskite film is an important issue. Currently, there are many techniques such as composition adjustment [17], process parameter control, and the use of additive [18] for preparing high-quality perovskite film. Additive engineering in perovskite films has been well investigated in PSCs. Among them, the polymeric molecules are usually used as an additive, because the specific functional groups and lone pair electrons on oxygen, sulfur, or nitrogen as Lewis bases in the main or side chain can effectively passivate defects of the perovskite [19–22]. Moreover, the polymers with a long chain can not only act as scaffolds of perovskite crystals but also cross-linking the perovskite grains to obtain the large crystal grains and smooth surface of the perovskite films [23,24]. Some of the literature has shown that adding a small amount of polymer to perovskites can effectively passivate defects and traps. [25,26].

The lab-scale PSCs, which show great achievement in device efficiency, typically use spin-coating techniques in an inert glovebox environment. However, the spin-coating technique has a low throughput, wastes a large amount of precursor solution, and is unsuitable for preparing large-area PSCs. To enable continuous manufacturing, many large-area coating methods have been developed, including slot die [27], blade coating [28–30], inkjet printing [31,32], vacuum deposition [33], and spray coating [34]. Among these scalable deposition technologies, the blade-coating method received more attention because it is compatible with roll-to-roll fabrication. In addition, the blade-coating method has the advantage of being a simple, cost-efficient, and low-temperature process. Unlike the spin-coating method, the blade-coating method can control the substrate temperature, the gap between the blade and substrate, and the coating speed for large-grain-size perovskite film [35].

In this study, a non-ionic surfactant, polyoxyethylene (20) sorbitan monolaurate (Tween 20), was added to the perovskite precursor solution [36]. The $MAPbI_3$ perovskite films were fabricated by the thermal-assisted blade-coating method. The results show that the crystalline domain size of the $MAPbI_3$ perovskite film can be controlled by adding Tween 20. Adding an appropriate amount of Tween 20 into the $MAPbI_3$ perovskite film also significantly enhances the radiative recombination. At the optimal Tween 20 (1.0 mM) concentration, the champion PSC demonstrated a PCE of 18.80%. This work gives an insight into the effect of surfactants in $MAPbI_3$ perovskite devices produced by the thermal-assisted blade-coating method for the large-area fabrication process.

2. Materials and Methods

2.1. Preparation of Materials

All reagents were analytical grade and used as received without further purifications. For preparation of the dense TiO_2 precursor solution, 1.0 mL of titanium diisopropoxide bis(acetylacetonate) was added in 39.0 mL of ethanol (CH_3CH_2OH, >99.8%, Sigma-Aldrich, St. Louis, MO, USA). The synthesis of TiO_2 paste was based on our previous study [37]. Briefly, 25.0 g of titanium isopropoxide ($Ti(OCH(CH_3)_2)_4$, >97%, Sigma-Aldrich, St. Louis, MO, USA) was added in 10.0 mL of 2-propanol ($(CH_3)_2CHOH$, IPA, >99.8%, STAREK, Taipei, Taiwan) while stirring. Next, TTIP/IPA solution was dropped into 90.0 mL of 3.5 M acetic acid (CH_3COOH, >99.7%, Sigma-Aldrich, St. Louis, MO, USA), cooled in an ice bath for 12 h, and then heated at 80 °C for 8 h. The pale yellow solution was transferred into an autoclave at 170 °C for 6 h to obtain TiO_2 nanoparticles. A total of 23.0 wt% of TiO_2 nanoparticles was diluted with α-terpineol ($C_{10}H_{18}O$, 90%, Merck, Darmstadt, Germany) and ethyl cellulose (ethoxyl content 48%, 22 cps, Acros Organics, Geel, Belgium). The pristine perovskite solution of 1.5 M CH_3NH_3I (MAI, >98%, FrontMaterials, Taipei, Taiwan) and 1.5 M lead iodide (PbI_2, 99.9985%, Alfa Aesar, Tewksbury, MA, USA) in a mixed solvent of DMSO (99.9%, ECHO)/GBL (≥99%, Acros Organics, Geel, Belgium) (90/10 v/v) was prepared. For Tween 20 perovskite solution, various concentrations of Tween 20 were added to the $MAPbI_3$ perovskite precursor solution, including 1.0, 2.0, and 3.0 mM, respectively. The preparation of hole transport material (HTM, spiro-OMeTAD, FrontMaterials, Taipei, Taiwan) was based on the previous work [38].

2.2. Fabrication of the $MAPbI_3$ Perovskite Solar Cells

The FTO glass (10 × 10 cm, 7 Ω/square, Ruilong, Miaoli, Taiwan) was ultrasonically cleaned with deionized water, acetone, IPA, followed by 10 min of UV–ozone treatment. Then, the dense TiO_2 was deposited on the FTO glass at 450 °C using the spray pyrolysis method. To deposit the mesoporous TiO_2 (mp-TiO_2) layer, the TiO_2 paste was on top of the dense TiO_2 using the screen-printing method, followed by 30 min of calcination at 500 °C to form the mp-TiO_2 layer. For the fabrication of the $MAPbI_3$ perovskite layer, a 2.5 × 5.0 cm FTO/dense TiO_2/mp-TiO_2 was preheated to 130 °C. A total of 30.0 µL of perovskite precursor solution was dropped on the top of the mp-TiO_2 layer under ambient atmosphere (30–40 %RH). Then, at 130 °C, the metal blade (ZUA 2000, Zehntner, Sissach, Switzerland) scraped excess solution for 3 min at a coating speed of 3.0 cm/s and a blade gap of 300 µm. The HTM solution was spin-coated on the perovskite layer at 2000 rpm for 30 s. A 100 nm thick silver electrode was deposited on the HTM using thermal evaporation with a 0.09 cm^2 metal mask.

2.3. Characterizations

The surface morphology of $MAPbI_3$ perovskite films was measured by atomic force microscopy (AFM) (Multimode2-U-NSV, Bruker, Billerica, MA, USA). Field-emission scanning electron microscopy (FE-SEM) images were obtained using a HITACHI (Tokyo, Japan) su8010 to observe samples' surface and cross-section morphology. XRD analysis was obtained using an X-ray diffractometer (D2 phaser, Bruker, Billerica, MA, USA) with Cu Kα (λ = 1.5418 Å) radiation. An ultraviolet–visible spectrophotometer (V-730, Jasco, Tokyo, Japan) was used to measure the optical properties of the $MAPbI_3$ perovskite film. The photoluminescence (PL) spectra and time-resolved photoluminescence (TRPL) spectra were recorded with a continuous 532 nm diode laser (LDH-D-TA-530, PicoQuant, Berlin, Germany). The TRPL–decay curves were recorded by a time-correlated single-photon counting (TCSPC) (TimeHarp 260, PicoQuant, Berlin, Germany) spectrometer. The current density–voltage (J-V) performances of various PSCs were measured using a digital source meter (Keithley 2400 Series, Keithley Instruments Inc., Cleveland, OH, USA) under AM 1.5 G simulated solar illumination (100 mW/cm^2, YCSS-50, Yamashita Denso Corp., Chiba, Japan). The light intensity was calibrated with a silicon reference cell (BS-520B, Bunkoukeiki Co., Ltd., Tokyo, Japan) with a KG-5 filter. To ensure the reliability and repeatability of data, average photovoltaic parameters of each PSC device were obtained from 18 devices. The external quantum efficiency (EQE) spectra were recorded from 300 to 900 nm using an IPCE spectrometer (EQE-R-3011, Enli Technology Co. Ltd., Kaohsiung, Taiwan).

3. Results and Discussion

The surface morphologies of various $MAPbI_3$ perovskite films coated on FTO-coated glass/TiO_2 were characterized by AFM. The chemical structure of the surfactant Tween 20 is shown in Figure 1a. The large-sized perovskite spherulite films can be prepared using the blade-coating method due to the rapid solvent evaporation during the heating [30,39]. The spherulites can be observed in all the perovskite films, as shown in Figure 1b–e, and their RMS and Rs values are also summarized in Table S1. The spherulite size of the pristine perovskite film (0.0 mM) is ~4.0 µm (Figure 1b). When the concentration of the Tween 20 reached 1.0 mM, the size of the spherulites reached ~6.0 µm (Figure 1c), which indicated that the small amount of the Tween 20 could increase the crystal size and decrease the grain boundaries. When the Tween 20 concentration was further increased to 2.0 and 3.0 mM, the spherulite size reduced significantly (Figure 1d,e). The long-chain alkyl groups present in Tween 20 can bridge the perovskite grains by forming a polymer-perovskite composite cross-linker, which produces a large crystal size, defect passivation, and the grain boundaries of the perovskite films. However, the excess Tween 20 addition causes restricted spherulite growth [21,22,40]. In addition, the most uniform surface is obtained by adding 1 mM Tween 20 into the perovskite precursor from the Ra and RMS result of the AFM measurement.

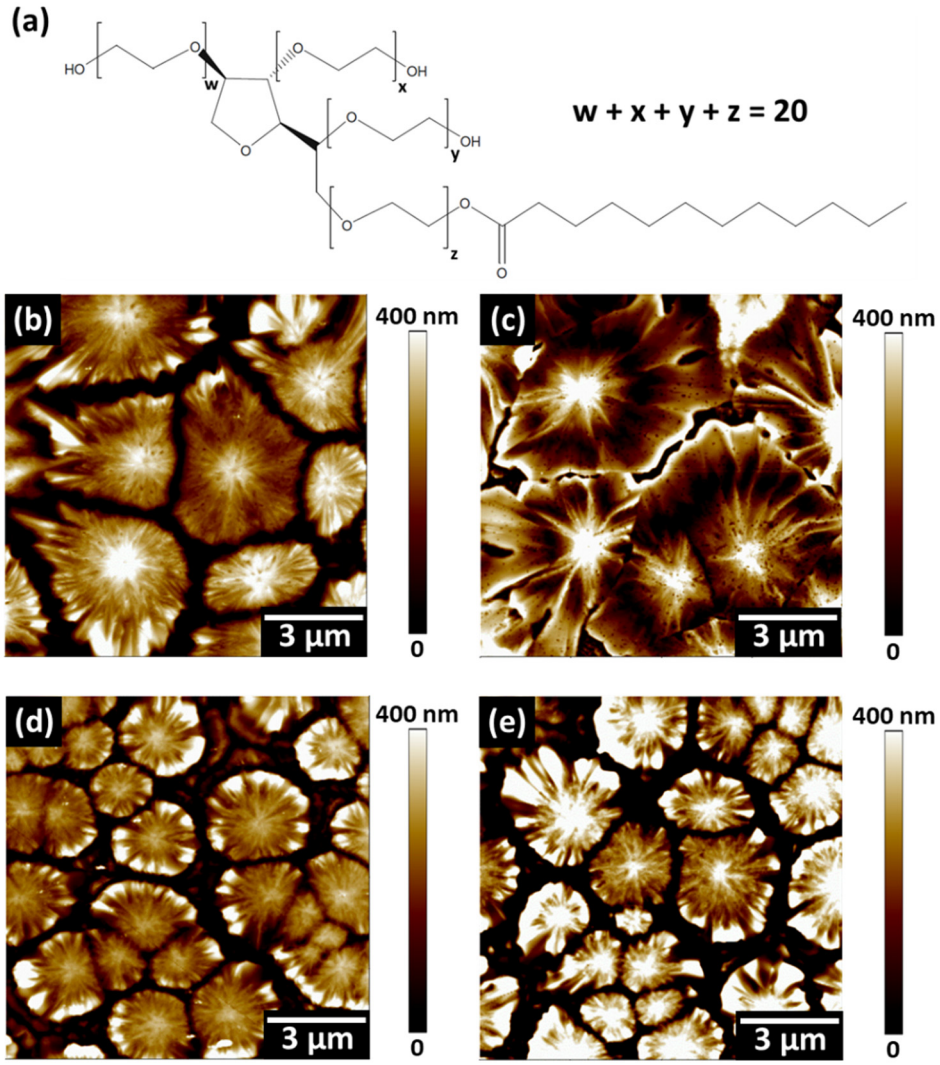

Figure 1. (**a**) Chemical structure of the surfactant Tween 20 and the AFM images of perovskite films with various Tween 20 concentrations, including (**b**) 0.0, (**c**) 1.0, (**d**) 2.0, and (**e**) 3.0 mM.

Figure 2a shows the UV–vis absorption spectra of pristine, 1.0, 2.0, and 3.0 mM Tween 20 perovskite films. The absorbance of the 1.0 mM Tween 20 perovskite film was enhanced due to the large-sized perovskite spherulites. However, the absorbance of the 2.0 and 3.0 mM Tween 20 perovskite films were reduced, which could be attributed to the reduction size of the spherulite sizes [41]. The XRD patterns of the four $MAPbI_3$ perovskite films are shown in Figure 2b (the standard XRD patterns of $MAPbI_3$ from the database are also shown in Figure S1). The pristine perovskite film showed two diffraction peaks which could be assigned to the (200) and (400) planes. The same results also appeared in our previous work [30]. Here, the fabrication process of the perovskite film affected the preferred crystal orientation of the perovskite, especially during a high-temperature process. It is worth noting that when the Tween 20 concentration was 1.0 mM, the peaks of the (200) and (400) planes were substantially reduced and replaced by the peaks of the (110) and (220) planes. These results showed that adding non-ionic surfactants with long alkyl chains and hydroxyl groups to perovskite films could tune their crystallinity behavior. The hydroxyl group has hydrophilic properties that support the crystal growth of perovskite [42]. On the other hand, the long alkyl chains with hydrophobic properties wrap around the perovskite crystals [43]. However, when excessive Tween 20 was added to the perovskite film, the crystallinity and grain size decreased (Figure S2). The growth of the spherulites was limited because the Tween 20 surrounded the spherulites.

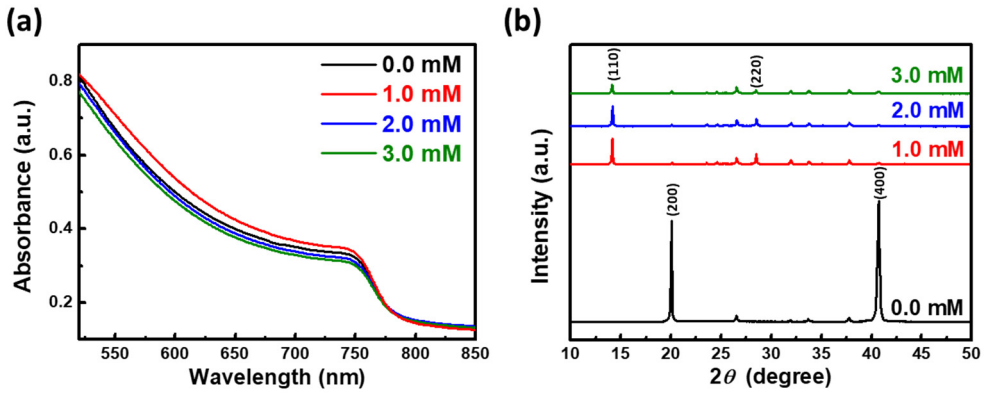

Figure 2. (**a**) UV–vis absorption spectra and (**b**) XRD patterns of pristine, 1.0, 2.0, and 3.0 mM Tween 20 perovskite films.

The steady-state photoluminescence (PL) spectra of various $MAPbI_3$ perovskite film/glass samples were also investigated in detail. As indicated in Figure 3a, the 1.0 and 2.0 mM Tween 20 perovskite films showed a higher PL peak intensity under the same excitation condition due to the reduction in non-radiative losses in the perovskite film. The corresponding time-resolved photoluminescence (TRPL) decay plots were performed to estimate the charge carrier dynamics of various $MAPbI_3$ perovskite films (Figure 3b). Herein, a 765 nm single-wavelength light was used as an excitation source. The PL–decay curves were fitted with a bi-exponential decay model [44]:

$$F(t) = A\exp\left(-\frac{t}{\tau_1}\right) + B\exp\left(-\frac{t}{\tau_2}\right) \quad (1)$$

where A and B are the weight fractions, τ_1 and τ_2 are the fast decay lifetime and the slow decay lifetime, respectively. For the average decay lifetime (τ_{avg}) calculation, the equation is shown below, and the results are listed in Table 1.

$$\tau_{avg} = (A\tau_1 + B\tau_2)/(A + B) \quad (2)$$

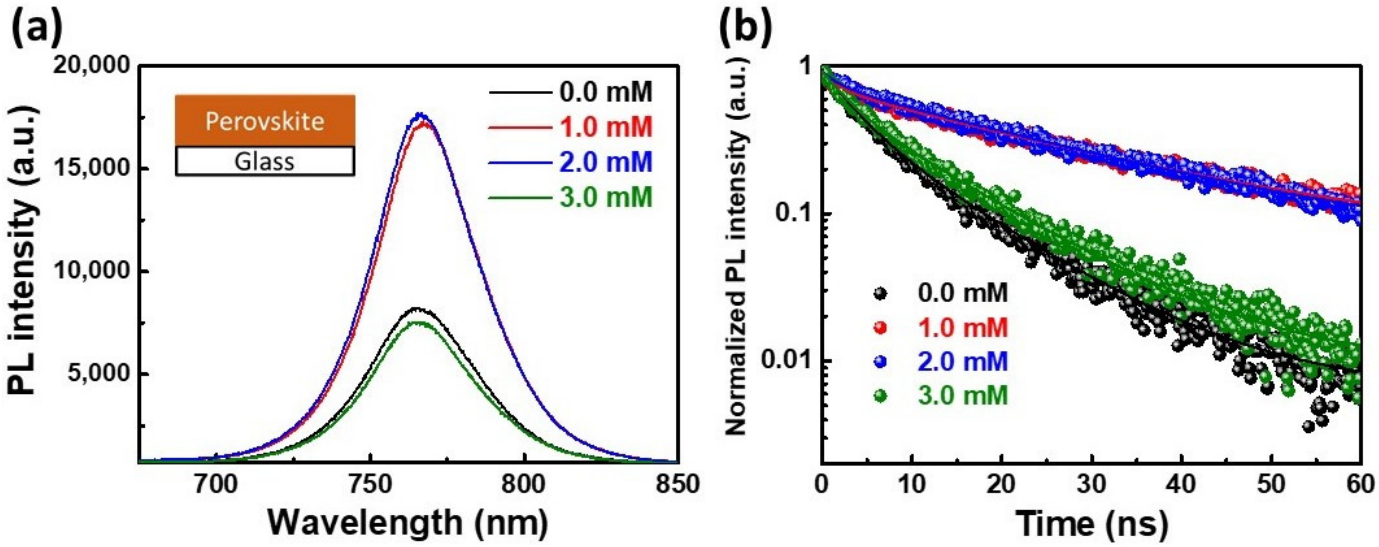

Figure 3. (**a**) PL and (**b**) TRPL spectra of pristine, 1.0, 2.0, and 3.0 mM Tween 20 perovskite films.

Table 1. Summary of the fast decay lifetime (τ_1), the slow decay lifetime (τ_2), and the average decay lifetime (τ_{avg}) for $MAPbI_3$ perovskite films/glasses.

Tween 20 Concentration (mM)	A (%)	τ_1 (ns)	B (%)	τ_2 (ns)	τ_{avg} (ns)
0.0	36.3	13.0	63.7	4.4	7.5
1.0	76.3	28.5	23.7	3.2	22.5
2.0	78.8	26.6	21.2	2.8	21.5
3.0	47.8	14.2	52.2	4.4	9.0

The τ_{avg} values of the 1.0 and 2.0 mM Tween 20 films increased to 22.5 and 21.5 ns, respectively. According to the above results, the appropriate amount (1.0 mM) of Tween 20 could form a large crystal size and passivate the defect and grain boundaries of the perovskite films, which can suppress carrier trapping, recombination, and significantly improve the slow decay process [40].

The schematic diagram and cross-section SEM image of the PSCs are shown in Figure 4a and Figure S3, respectively. It has the structure of an FTO/dense TiO_2/mesoporous TiO_2/$MAPbI_3$ perovskite layer/spiro-OMeTAD/Ag electrode. The photovoltaic characteristics of the PSCs with various concentrations of Tween 20 in the perovskite films are shown in Figure 4b and Table 2. When the Tween 20 concentration increased from 0.0 to 1.0 mM, the short-circuit current density (J_{SC}) increased from 19.89 to 21.46 mA/cm^2, leading to a PCE of 15.75%. The improved photocurrent was due to the high absorption and uniform surface morphology (from Table S1) of the perovskite films with an appropriate amount of surfactant. On the contrary, the PCE of the PSCs with 3.0 mM Tween 20 remarkably decreased to 14.59%. When the Tween 20 concentration was increased to 3.0 mM, it led to the highest short-circuit current density (J_{SC}) at 21.6 mA/cm^2. The possible reason for the decrease in the PCE was the decreased crystal size due to an excess amount of Tween 20. The J-V curves of the champion pristine and 1.0 mM Tween 20 PSCs are shown in Figure 4c. For the pristine device, the J-V parameters were J_{SC} = 20.30 mA/cm^2, V_{OC} = 1.031 V, FF = 69.3%, with a PCE of 14.51%, respectively. The maximum performances of the 1.0 mM Tween 20 PSC were J_{SC} = 22.90 mA/cm^2, V_{OC} = 1.059 V, FF = 72.6%, with a PCE of 17.60%, respectively. The EQE spectra (Figure 4d) show that the integrated J_{SC} of the 1.0 mM Tween 20 PSC is 21.00 mA/cm^2.

Herein, the thermal-assisted blade coating optimized the 1.0 mM Tween 20 perovskite films fabrication temperature to obtain the optimized grain size and device performance. It was found that the largest grain size and the best device efficiency were both obtained at 120 °C (Figure S4). This temperature was lower than the applied temperature of 130 °C for the one prepared without the Tween 20, as shown in our previous study [45,46]. This finding revealed that the addition of Tween 20 contributed to the growth of the perovskite crystal arrangement, leading to a lower optimal film-forming temperature.

To further illustrate the influence of the thermal-assisted blade-coating and spin-coating methods on the $MAPbI_3$ perovskite device characteristics, the 1.0 mM Tween 20 perovskite films were prepared separately using the two different methods, and their surface morphologies are shown in Figure S5. Evidently, the thermal-assisted blade-coating method effectively reduced the grain boundaries of the perovskite films and had a larger domain size than that obtained by the spin-coating process. Figure 5a demonstrates the J-V curves of the perovskite device prepared by the two different methods. The spin-coated PSC exhibited a J_{SC} of 22.63 mA/cm^2, V_{OC} of 1.060 V, FF of 66.92%, and PCE of 16.05%. In contrast, the blade-coated PSC achieved an efficiency of 18.80% and showed no apparent hysteresis (Figure 5b).

As previously mentioned, the thermal-assisted blade coating is suitable for fabricating large-area devices due to its coating uniformity. This advantage prompted us to fabricate PSCs with various active areas (Figure 6a), including 3 × 3, 4 × 4, 5 × 5, 6 × 6, and 7 × 7 mm^2. The active areas versus the PCE of the 1.0 mM Tween 20 PSCs prepared

by the two different methods are shown in Figure 6b,c. When the active area increased, the performance of the spin-coated PSC dropped dramatically, with a large standard deviation. However, the efficiency of large-area devices fabricated by the thermal-assisted blade-coating method was much more stable, meaning that this method produced high uniformity. These results were also in line with expectations.

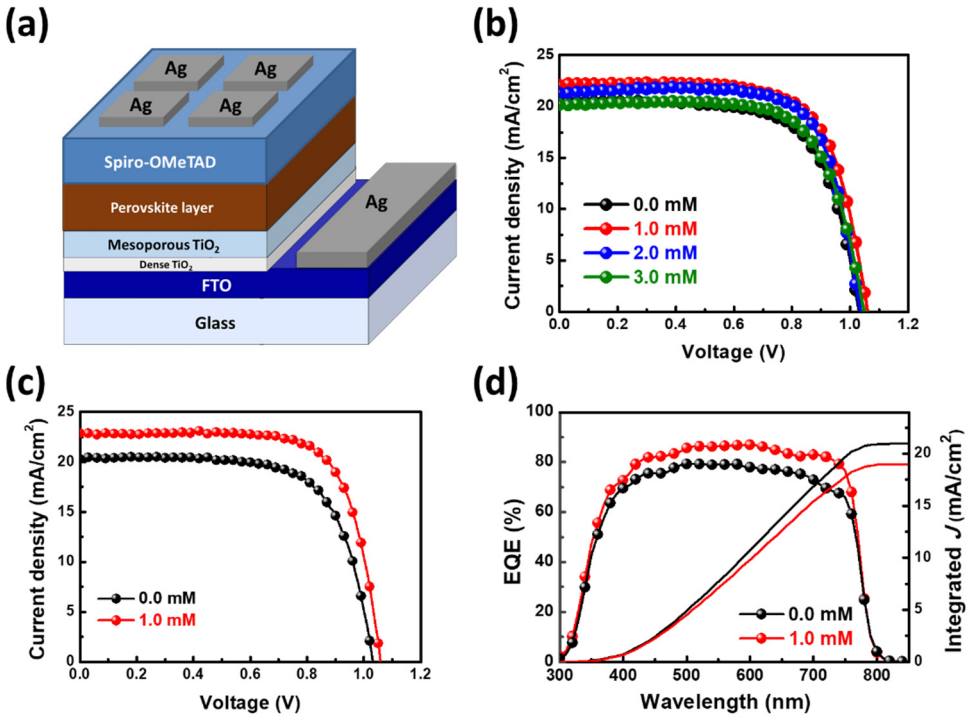

Figure 4. (**a**) The schematic diagram of PSC. (**b**) J-V curves of pristine, 1.0, 2.0, and 3.0 mM Tween 20 PSCs. (**c**) J-V curves and (**d**) EQE spectra of champion pristine and 1.0 mM Tween 20 PSCs.

Table 2. Photovoltaic characteristics of pristine, 1.0, 2.0, and 3.0 mM Tween 20 PSCs. The average device parameters for 18 cells of same configuration are presented.

Tween 20 Concentration (mM)	J_{SC} (mA/cm^2)	V_{OC} (V)	FF (%)	PCE (%)	Champion PCE (%)
0.0	19.89 ± 0.87	1.022 ± 0.020	67.8 ± 1.7	13.79 ± 0.82	14.51
1.0	21.46 ± 0.46	1.035 ± 0.022	70.9 ± 1.2	15.75 ± 0.62	17.60
2.0	21.02 ± 0.27	1.022 ± 0.025	69.5 ± 2.9	15.45 ± 0.75	16.23
3.0	20.03 ± 1.18	1.046 ± 0.023	69.6 ± 0.7	14.59 ± 0.96	14.94

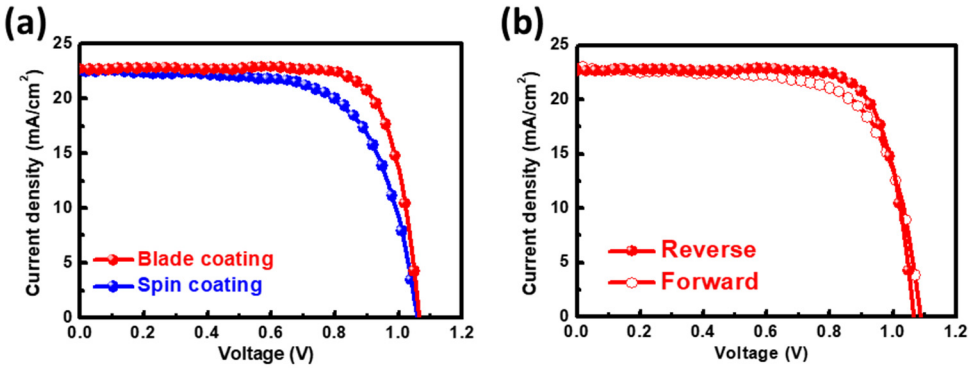

Figure 5. (**a**) J-V curves of the 1.0 mM Tween 20 PSCs prepared by the two different methods. (**b**) Hysteresis measurement of 1.0 mM Tween 20 PSCs prepared by the thermal-assisted blade-coating method.

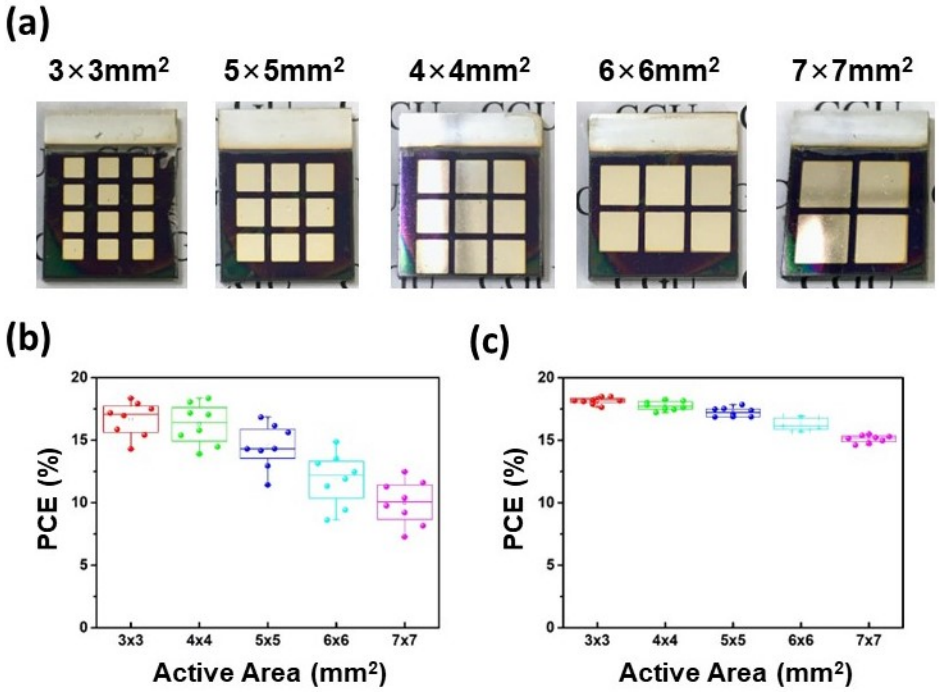

Figure 6. (**a**) Photos of perovskite devices with various active areas. (**b**) The area-dependent statistical performance of 1.0 mM Tween 20 PSCs fabricated by (**b**) the spin-coating method and (**c**) the thermal-assisted blade-coating method.

For the stability study, the 1.0 mM Tween 20 perovskite films prepared by the two methods were treated at 90 and 110 °C for 12 h, respectively. Both films were stable under 90 °C. However, the spin-coated film showed the significant production of a PbI_2 peak, revealing that the perovskite film prepared by the thermal-assisted blade-coating method had less grain boundary and better thermal stability (Figure 7a). Moreover, the 1.0 mM Tween 20 PSCs prepared by the two different fabrication methods were exposed to the ambient atmosphere (~45% relative humidity, 25 °C) for 100 days, as shown in Figure 7b. The PSC fabricated by the thermal-assisted blade-coating method retained 72% of its initial PCE after 100 days of exposure without encapsulation. In contrast, the spin-coated device only retained 53% of its initial PCE under the same condition. The excellent long-term stability reveals that perovskite film prepared by the thermal-assisted blade-coating method can reduce grain boundaries and further improve perovskite films' crystal quality.

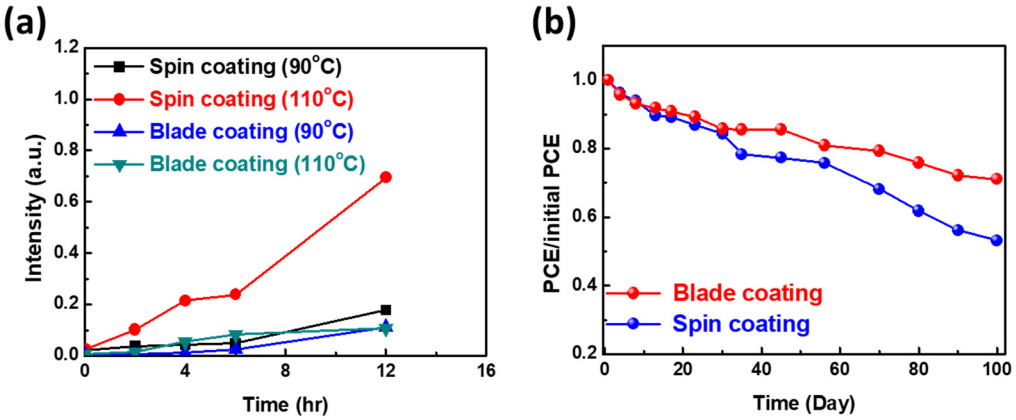

Figure 7. (**a**) Intensity ratio of PbI_2 formed in the $MAPbI_3$ perovskite film under thermal treatment and (**b**) long-term stability of PSCs fabricated by the two methods under ambient atmosphere (~45% relative humidity, 25 °C).

4. Conclusions

In conclusion, the effects of various concentrations of surfactant Tween 20 on $MAPbI_3$ perovskite films prepared by thermal-assisted blade coating, including surface morphology, optical properties, crystal structure, and charge carrier dynamics, were systematically studied. The 1.0 mM Tween 20 perovskite film demonstrated a higher PL intensity and a longer carrier lifetime due to defect passivation. The champion PSC provided a PCE of 18.80%. Finally, the larger area PSC prepared by the thermal-assisted blade-coating method showed a higher performance and better ambient stability than the spin-coated devices.

Supplementary Materials: The following supporting information can be downloaded at: https://www.mdpi.com/article/10.3390/nano12152651/s1. Figure S1: The XRD patterns of the perovskite films with different concentration Tween 20, and the reference standard for MAPbI3 and FTO; Figure S2: The grain size of perovskite films without and with different Tween 20 concentrations; Figure S3: FE-SEM images of cross-section PSC (a) without and with 1.0 mM Tween 20; Figure S4: The grain size of perovskite films with 1.0 mM Tween 20 with different fabrication temperatures; Figure S5: The top-view surface morphologies of perovskite film with 1.0 mM Tween 20 under two different preparation methods, including (a) spin coating and (b) thermal assisted blade coating method; Table S1: The morphological characteristics (Ra and RMS) of perovskite films with various Tween 20 concentrations by using AFM measurement.

Author Contributions: S.-H.C. (Shun-Hsiang Chan), C.-C.T., W.-H.C. and S.-H.C. (Shih-Hsuan Chen) performed the experiments and analysis, as well as writing and editing the manuscript. K.-M.L., V.S., J.-F.H., C.-Y.L. and M.-C.W. supervised the work and reviewed the manuscript. All authors have read and agreed to the published version of the manuscript.

Funding: This research was funded by the Ministry of Science and Technology, Taiwan (Grant Number MOST 108-2628-E-182-003-MY3 and 110-2113-M-008-001), Chang Gung University (QZRPD181), and Chang Gung Memorial Hospital, Linkou, Taiwan (CMRPD2M0041).

Institutional Review Board Statement: Not applicable.

Informed Consent Statement: Not applicable.

Data Availability Statement: Not applicable.

Conflicts of Interest: The authors declare no conflict of interest.

References

1. Yue, L.; Yan, B.; Attridge, M.; Wang, Z. Light absorption in perovskite solar cell: Fundamentals and plasmonic enhancement of infrared band absorption. *Sol. Energy* **2016**, *124*, 143–152. [CrossRef]
2. Agbaoye, R.O.; Akinlami, J.O.; Afolabi, T.A.; Adebayo, G.A. Unraveling the Stable Phase, High Absorption Coefficient, Optical and Mechanical Properties of Hybrid Perovskite CH3NH3PbxMg1–xI3: Density Functional Approach. *J. Inorg. Organomet. Polym. Mater.* **2020**, *30*, 299–309. [CrossRef]
3. You, Y.-J.; Saeed, M.A.; Shafian, S.; Kim, J.; Hyeon Kim, S.; Kim, S.H.; Kim, K.; Shim, J.W. Energy recycling under ambient illumination for internet-of-things using metal/oxide/metal-based colorful organic photovoltaics. *Nanotechnology* **2021**, *32*, 465401. [CrossRef] [PubMed]
4. Saeed, M.A.; Cheng, S.; Biswas, S.; Kim, S.H.; Kwon, S.-K.; Kim, H.; Kim, Y.-H.; Shim, J.W. Remarkably high performance of organic photovoltaic devices with 3,9-bis(2-methylene-(3-(1,1-dicyanomethylene)-indanone))-5,5,11,11-tetrakis(4-hexyl metaphenyl)-dithieno[2,3-d:2′,3′-d′]-s-indaceno[1,2-b:5,6-b′]dithiophene)-ethylhexyloxy] photoactive acceptor under halogen light illumination. *J. Power Sources* **2022**, *518*, 230782. [CrossRef]
5. Kim, S.H.; Park, C.H.; Saeed, M.A.; Ko, D.-H.; Lee, J.-H.; Shim, J.W. β-cyclodextrin–polyacryloyl hydrazide-based surface modification for efficient electron-collecting electrodes of indoor organic photovoltaics. *J. Mater. Res. Technol.* **2022**, *16*, 1659–1666. [CrossRef]
6. Yoo, J.J.; Seo, G.; Chua, M.R.; Park, T.G.; Lu, Y.; Rotermund, F.; Kim, Y.-K.; Moon, C.S.; Jeon, N.J.; Correa-Baena, J.-P.; et al. Efficient perovskite solar cells via improved carrier management. *Nature* **2021**, *590*, 587–593. [CrossRef] [PubMed]
7. Chen, W.; Liu, S.; Li, Q.; Cheng, Q.; He, B.; Hu, Z.; Shen, Y.; Chen, H.; Xu, G.; Ou, X.; et al. High-Polarizability Organic Ferroelectric Materials Doping for Enhancing the Built-In Electric Field of Perovskite Solar Cells Realizing Efficiency over 24%. *Adv. Mater.* **2022**, *34*, 2110482. [CrossRef]
8. Snaith, H.J. Perovskites: The Emergence of a New Era for Low-Cost, High-Efficiency Solar Cells. *J. Phys. Chem. Lett.* **2013**, *4*, 3623–3630. [CrossRef]

9. Heshmati, N.; Mohammadi, M.R.; Abachi, P.; Martinez-Chapa, S.O. Low-cost air-stable perovskite solar cells by incorporating inorganic materials. *New J. Chem.* **2021**, *45*, 788–795. [CrossRef]
10. Qiu, L.; Dong, L.; Mei, D.; Chen, W.-H.; Song, L.; Wang, J.; Zou, J.; Jiang, P.-C.; Du, P.; Xiong, J. A simple fabrication of high efficiency planar perovskite solar cells: Controlled film growth with methylammonium iodide and green antisolvent sec-butyl alcohol. *J. Mater. Chem. C* **2020**, *8*, 12560–12567. [CrossRef]
11. Shaw, B.K.; Castillo-Blas, C.; Thorne, M.F.; Ríos Gómez, M.L.; Forrest, T.; Lopez, M.D.; Chater, P.A.; McHugh, L.N.; Keen, D.A.; Bennett, T.D. Principles of melting in hybrid organic–inorganic perovskite and polymorphic ABX3 structures. *Chem. Sci.* **2022**, *13*, 2033–2042. [CrossRef] [PubMed]
12. Pan, J.; Zhang, X.; Zheng, Y.; Xiang, W. Morphology control of perovskite film for efficient CsPbIBr2 based inorganic perovskite solar cells. *Sol. Energy Mater. Sol. Cells* **2021**, *221*, 110878. [CrossRef]
13. Chen, F.; Ma, Z.; Ye, L.; Ma, T.; Zhang, T.; Zhang, Y.; Huang, H. Macroscopic Spontaneous Polarization and Surface Oxygen Vacancies Collaboratively Boosting CO_2 Photoreduction on BiOIO3 Single Crystals. *Adv. Mater.* **2020**, *32*, 1908350. [CrossRef]
14. Fang, Z.; Wang, L.; Mu, X.; Chen, B.; Xiong, Q.; Wang, W.D.; Ding, J.; Gao, P.; Wu, Y.; Cao, J. Grain Boundary Engineering with Self-Assembled Porphyrin Supramolecules for Highly Efficient Large-Area Perovskite Photovoltaics. *J. Am. Chem. Soc.* **2021**, *143*, 18989–18996. [CrossRef] [PubMed]
15. Wu, J.; Li, Y.; Li, Y.; Xie, W.; Shi, J.; Li, D.; Cheng, S.; Meng, Q. Using hysteresis to predict the charge recombination properties of perovskite solar cells. *J. Mater. Chem. A* **2021**, *9*, 6382–6392. [CrossRef]
16. Kumar, A.; Rana, A.; Vashistha, N.; Garg, K.K.; Singh, R.K. Defect states influencing hysteresis and performance of perovskite solar cells. *Sol. Energy* **2020**, *211*, 345–353. [CrossRef]
17. Hu, C.; Bai, Y.; Xiao, S.; Zhang, T.; Meng, X.; Ng, W.K.; Yang, Y.; Wong, K.S.; Chen, H.; Yang, S. Tuning the A-site cation composition of FA perovskites for efficient and stable NiO-based p–i–n perovskite solar cells. *J. Mater. Chem. A* **2017**, *5*, 21858–21865. [CrossRef]
18. Pereyra, C.; Xie, H.; Lira-Cantu, M. Additive engineering for stable halide perovskite solar cells. *J. Energy Chem.* **2021**, *60*, 599–634. [CrossRef]
19. Lan, Y.; Wang, Y.; Song, Y. Efficient flexible perovskite solar cells based on a polymer additive. *Flex. Print. Electron.* **2020**, *5*, 014001. [CrossRef]
20. Fairfield, D.J.; Sai, H.; Narayanan, A.; Passarelli, J.V.; Chen, M.; Palasz, J.; Palmer, L.C.; Wasielewski, M.R.; Stupp, S.I. Structure and chemical stability in perovskite–polymer hybrid photovoltaic materials. *J. Mater. Chem. A* **2019**, *7*, 1687–1699. [CrossRef]
21. Wang, D.; Zhang, L.; Deng, K.; Zhang, W.; Song, J.; Wu, J.; Lan, Z. Influence of Polymer Additives on the Efficiency and Stability of Ambient-Air Solution-Processed Planar Perovskite Solar Cells. *Energy Technol.* **2018**, *6*, 2380–2386. [CrossRef]
22. Mei, Y.; Sun, M.; Liu, H.; Li, X.; Wang, S. Polymer additive assisted crystallization of perovskite films for high-performance solar cells. *Org. Electron.* **2021**, *96*, 106258. [CrossRef]
23. Han, T.-H.; Lee, J.-W.; Choi, C.; Tan, S.; Lee, C.; Zhao, Y.; Dai, Z.; De Marco, N.; Lee, S.-J.; Bae, S.-H.; et al. Perovskite-polymer composite cross-linker approach for highly-stable and efficient perovskite solar cells. *Nat. Commun.* **2019**, *10*, 520. [CrossRef] [PubMed]
24. Zhao, Y.; Wei, J.; Li, H.; Yan, Y.; Zhou, W.; Yu, D.; Zhao, Q. A polymer scaffold for self-healing perovskite solar cells. *Nat. Commun.* **2016**, *7*, 10228. [CrossRef] [PubMed]
25. Liu, K.; Liang, Q.; Qin, M.; Shen, D.; Yin, H.; Ren, Z.; Zhang, Y.; Zhang, H.; Fong, P.W.K.; Wu, Z.; et al. Zwitterionic-Surfactant-Assisted Room-Temperature Coating of Efficient Perovskite Solar Cells. *Joule* **2020**, *4*, 2404–2425. [CrossRef]
26. Deng, Y.; Zheng, X.; Bai, Y.; Wang, Q.; Zhao, J.; Huang, J. Surfactant-controlled ink drying enables high-speed deposition of perovskite films for efficient photovoltaic modules. *Nat. Energy* **2018**, *3*, 560–566. [CrossRef]
27. Li, J.; Dagar, J.; Shargaieva, O.; Flatken, M.A.; Köbler, H.; Fenske, M.; Schultz, C.; Stegemann, B.; Just, J.; Többens, D.M.; et al. 20.8% Slot-Die Coated MAPbI3 Perovskite Solar Cells by Optimal DMSO-Content and Age of 2-ME Based Precursor Inks. *Adv. Energy Mater.* **2021**, *11*, 2003460. [CrossRef]
28. Marques, A.S.; Faria, R.M.; Freitas, J.N.; Nogueira, A.F. Low-Temperature Blade-Coated Perovskite Solar Cells. *Ind. Eng. Chem. Res.* **2021**, *60*, 7145–7154. [CrossRef]
29. Jin, Z.; Zhang, Z.; Xiu, J.; Song, H.; Gatti, T.; He, Z. A critical review on bismuth and antimony halide based perovskites and their derivatives for photovoltaic applications: Recent advances and challenges. *J. Mater. Chem. A* **2020**, *8*, 16166–16188. [CrossRef]
30. Lee, K.-M.; Chan, S.-H.; Hou, M.-Y.; Chu, W.-C.; Chen, S.-H.; Yu, S.-M.; Wu, M.-C. Enhanced efficiency and stability of quasi-2D/3D perovskite solar cells by thermal assisted blade coating method. *Chem. Eng. J.* **2021**, *405*, 126992. [CrossRef]
31. Pendyala, N.K.; Magdassi, S.; Etgar, L. Fabrication of Perovskite Solar Cells with Digital Control of Transparency by Inkjet Printing. *ACS Appl. Mater. Interfaces* **2021**, *13*, 30524–30532. [CrossRef]
32. Schackmar, F.; Eggers, H.; Frericks, M.; Richards, B.S.; Lemmer, U.; Hernandez-Sosa, G.; Paetzold, U.W. Perovskite Solar Cells with All-Inkjet-Printed Absorber and Charge Transport Layers. *Adv. Mater. Technol.* **2021**, *6*, 2000271. [CrossRef]
33. Feng, J.; Jiao, Y.; Wang, H.; Zhu, X.; Sun, Y.; Du, M.; Cao, Y.; Yang, D.; Liu, S. High-throughput large-area vacuum deposition for high-performance formamidine-based perovskite solar cells. *Energy Environ. Sci.* **2021**, *14*, 3035–3043. [CrossRef]
34. Bishop, J.E.; Smith, J.A.; Lidzey, D.G. Development of Spray-Coated Perovskite Solar Cells. *ACS Appl. Mater. Interfaces* **2020**, *12*, 48237–48245. [CrossRef]
35. Ernst, M.; Herterich, J.-P.; Margenfeld, C.; Kohlstädt, M.; Würfel, U. Multilayer Blade-Coating Fabrication of Methylammonium-Free Perovskite Photovoltaic Modules with 66 cm^2 Active Area. *Sol. RRL* **2022**, *6*, 2100535. [CrossRef]

36. Liu, X.; Guo, X.; Lv, Y.; Hu, Y.; Fan, Y.; Lin, J.; Liu, X.; Liu, X. High Brightness and Enhanced Stability of $CsPbBr_3$-Based Perovskite Light-Emitting Diodes by Morphology and Interface Engineering. *Adv. Opt. Mater.* **2018**, *6*, 1801245. [CrossRef]
37. Wu, M.-C.; Chan, S.-H.; Lee, K.-M.; Chen, S.-H.; Jao, M.-H.; Chen, Y.-F.; Su, W.-F. Enhancing the efficiency of perovskite solar cells using mesoscopic zinc-doped TiO_2 as the electron extraction layer through band alignment. *J. Mater. Chem. A* **2018**, *6*, 16920–16931. [CrossRef]
38. Liu, D.; Kelly, T.L. Perovskite solar cells with a planar heterojunction structure prepared using room-temperature solution processing techniques. *Nat. Photonics* **2014**, *8*, 133–138. [CrossRef]
39. Bi, Z.; Rodríguez-Martínez, X.; Aranda, C.; Pascual-San-José, E.; Goñi, A.R.; Campoy-Quiles, M.; Xu, X.; Guerrero, A. Defect tolerant perovskite solar cells from blade coated non-toxic solvents. *J. Mater. Chem. A* **2018**, *6*, 19085–19093. [CrossRef]
40. Ho, C.-M.; Wu, M.-C.; Chen, S.-H.; Chang, Y.-H.; Lin, T.-H.; Jao, M.-H.; Chan, S.-H.; Su, W.-F.; Lee, K.-M. High-Performance Stable Perovskite Solar Cell via Defect Passivation with Constructing Tunable Graphitic Carbon Nitride. *Solar RRL* **2021**, *5*, 2100257. [CrossRef]
41. Hou, X.; Huang, S.; Ou-Yang, W.; Pan, L.; Sun, Z.; Chen, X. Constructing Efficient and Stable Perovskite Solar Cells via Interconnecting Perovskite Grains. *ACS Appl. Mater. Interfaces* **2017**, *9*, 35200–35208. [CrossRef] [PubMed]
42. Kim, H.; Hong, J.; Kim, C.; Shin, E.-Y.; Lee, M.; Noh, Y.-Y.; Park, B.; Hwang, I. Impact of Hydroxyl Groups Boosting Heterogeneous Nucleation on Perovskite Grains and Photovoltaic Performances. *J. Phys. Chem. C* **2018**, *122*, 16630–16638. [CrossRef]
43. Feng, W.; Zhang, C.; Zhong, J.-X.; Ding, L.; Wu, W.-Q. Correlating alkyl chain length with defect passivation efficacy in perovskite solar cells. *Chem. Commun.* **2020**, *56*, 5006–5009. [CrossRef]
44. Kirchartz, T.; Márquez, J.A.; Stolterfoht, M.; Unold, T. Photoluminescence-Based Characterization of Halide Perovskites for Photovoltaics. *Adv. Energy Mater.* **2020**, *10*, 1904134. [CrossRef]
45. Lee, K.-M.; Lai, C.-H.; Chu, W.-C.; Chan, S.-H.; Suryanarayanan, V. Thermal assisted blade coating methylammonium lead iodide films with non-toxic solvent precursors for efficient perovskite solar cells and sub-module. *Sol. Energy* **2020**, *204*, 337–345. [CrossRef]
46. Lee, K.-M.; Chiu, W.-H.; Tsai, Y.-H.; Wang, C.-S.; Tao, Y.-T.; Lin, Y.-D. High-performance perovskite solar cells based on dopant-free hole-transporting material fabricated by a thermal-assisted blade-coating method with efficiency exceeding 21%. *Chem. Eng. J.* **2022**, *427*, 131609. [CrossRef]